Chapter 3 : Recursive Bayesian Regularization for Ultrasound Strain Imaging

This chapter describes a recursive Bayesian regularization algorithm applied during ultrasound displacement estimation to improve the quality by reducing artifacts and improving the signal-to-noise in carotid strain images. First, we describe regularization's role in the block-matching approach to deformable image registration. Then we review regularization algorithms that have been implemented in the literature. Next, we describe the iterative probabilistic approach taken in this work. Finally, we present results on simulations, phantoms, and carotid strain image case studies. [1]

---

1 This chapter is adapted from McCormick, M. Rubert, N. and Varghese, T. *Bayesian Regularization Applied to Ultrasound Strain Imaging*. IEEE Transactions in Biomedical Engineering. 2011. In Press.

3.1 Improvement of strain image quality with regularization

The deformable image registration problem is common in medical imaging [1, 2]. It is used to monitor tumor growth, compensate for patient motion, register to a common atlas, etc. In the context of ultrasound strain imaging, estimating local displacements is the first step in a two stage process; in the second step strains are calculated from the estimated displacements. In some cases strain is estimated iteratively along with the displacements in order to improve the quality of strain estimation [3, 4, 5], but all algorithms take this general form.

In simple block-matching image registration methods, the registration of a block is isolated to the given block. Motion of the block is local, and motion of surrounding regions is not considered in determination of the block's displacement. Regularization methods enable prior estimated displacements and the success in tracking of deformations surrounding regions to influence the local displacement estimate.

Most regularization routines fit into a cost function paradigm. Without regularization, the estimated displacement, $\hat{\mathbf{u}}_{\mathbf{x}}$, can be formulated as

$$\hat{\mathbf{u}}_{\mathbf{x}} = \arg\min_{\mathbf{u}_{\mathbf{x}}} E_s(\mathbf{u}_{\mathbf{x}})$$

Eqn. 3.1

Where E_s is a similarity metric term, and examples include the sum of squared differences, negative of the correlation coefficient, etc. When regularization is performed in a cost function paradigm, an additional term must be minimized.

$$\hat{\mathbf{u}}_{\mathbf{x}} = \arg\min_{\mathbf{u_x}}[E_s(\mathbf{u_x}) + \alpha \, E_c(\mathbf{u}_{\mathcal{N}_x}, E_s(\mathbf{u}_{\mathcal{N}_x}))]$$

Eqn. 3.2

Here E_c is a continuity term that depends on the neighboring displacements and the similarity metric at neighboring displacements. The parameter α determines the amount of regularization. A higher α will provide a greater weight to the displacement of surrounding displacements and increase the amount of regularization. Different algorithms implement their choice of E_s, E_c, and along with an optimization method to minimize the cost function.

The result of regularization is an improved displacement estimate since we can incorporate our *a priori* knowledge that the displacement is continuous. However, if the regularization parameter α is too large, excessive smoothing may be introduced causing a loss in spatial resolution and elimination of small features and a reduction in the dynamic range in the strain images. Regularization of this type is especially important for block-matching deformable image registration techniques where the motion model does not assume any continuity. Motion is considered to be a completely local phenomenon. This contrasts with B-spline, elastic body spline, or Finite Element Method (FEM) based deformable image registration methods [6, 7, 8, 9, 10]. In these methods, the motion model is such that a local point moves in concert with surrounding tissues.

While the B-spline deformable transform does not have the same difficulty that the block-matching methods have in enforcing local continuity, they both share a related problem since the B-Spline deformation basis functions are compactly supported. Both block-matching and B-spline deformable transforms do not enforce a diffeomorphic transform [11, 9]. A displacement

map that is diffeomorphic must be continuous, differentiable, and invertible [9]. A diffeomorphic transformation is a one-to-one mapping between the pre and post deformation image. In general, folding or tearing is not likely or possible in physical tissues, so diffeomorphic behavior should be enforced.

Peak-hopping errors in block-matching methods will also result in non-diffeomorphic displacement maps. Since regularization helps to enforce diffeomorphic behavior with block-matching methods, it helps to remove peak-hopping errors in addition to generally improving the motion estimates. The motion estimates are improved by addressing quantization and decorrelation noise as well as addressing the "aperture" problem [12]. The aperture problem recognizes that a block may not have derivatives in the image intensity in all directions, and it is difficult to determine displacement in directions where gradients are small.

3.2   Prior efforts in regularization

Peak hopping errors and degradation in the quality of the strain image result primarily from signal decorrelation [13, 14]. The source of signal decorrelation can be large axial deformations that distort the signal, reverberations, motion of tissue in the elevational direction relative to the probe, or undesirable physiological motion [15, 16].

Most approaches to address signal decorrelation can be placed in two categories. One strategy tries to reduce peak hopping by restricting the search region of a matching kernel. Tighter search regions are feasible when the center of the search region is initialized appropriately. Sometimes, *a priori* knowledge of the type of motion expected is used to initialize search regions. Hall et al. [17] described an implementation where the displacement is always assumed to be null at the transducer surface. This is a reasonable assumption since the transducer must always remain in contact with the tissue to generate an image and the stiffness of

transducer is much higher than the deformed soft tissue, so it is effectively a rigid body. Motion tracking starts from the transducer surface, and the displacement estimates are used to initialize search regions deeper into tissue. Basarab et al. [18] describe a similar strategy where search regions are propagated by displacement estimates starting from the center of the transducer. The points initialized are set in a "V" shaped front in order to better initialize lateral displacements since lateral displacements are often near zero at the transducer's center during freehand compression and increases towards the edges of the transducer.

Search region initialization strategies that do not depend on the presence of locations of zero displacement somewhere in the image use points or lines of high displacement estimation confidence. Instead of propagating search region centers axially from the transducer surface, estimates can be propagated laterally from an A-line of high confidence [19, 20] or diagonally [21]. Chen et al. have described a quality-guided algorithm that uses multiple seed points [22]. The initial seed points require a large search region, however, after initialization, these search regions are kept small. Displacements are estimated from neighbors adjacent to the seed with the search region centered at the seed's displacement. Among these neighbors and the other seed's neighbors, the location with the best quality metric is used to initialize the next set of search regions. The process proceeds iteratively until the entire image has been tracked, and search region initialization propagates from locations of highest tracking quality. The quality metric used in [22] was the normalized cross correlation coefficient value.

A weakness of the other search region initialization algorithms that the seeds algorithm overcomes is the presence of discontinuous locations. This can occur with a slip boundary along a tumor or the vessel wall of the carotid artery, for example. This weakness is also overcome by a coarse-to-fine scheme where displacements from a large kernel or low-pass filtered and sub-

sampled kernel initializes the center of the search region at progressively smaller kernel sizes to achieve a high resolution strain image [23, 24, 25, 26, 27, 18, 28]. This multi-resolution pyramid approach is commonly employed in many different types of registration problems. Since tracking in the coarse image can be performed on subsampled data, initialization is performed quickly. Also, robustness is improved because initialization occurs near the final solution and local minima in the high frequency speckle are avoided.

The second strategy to address decorrelation noise in ultrasound displacement estimation incorporates displacements from neighboring blocks into the displacement estimation equation. Filtering approaches remove noise but come at the cost of reduced strain dynamic range and spatial resolution. For example, a median filter can be used to remove outliers, [29]. During computation of strains from estimated displacement, a least squares fit to the displacement can be used to estimate the local slope in displacement [16]. A statistical model of the displacements can be taken and the Kalman filter used during estimation of the strain [20]. Alternatively, as mentioned previously, a cost function optimization approach can be taken involving a similarity metric term and a displacement continuity term. Both Jiang and Hall [30] and Rivaz [31] describe implementations of this approach that use dynamic programming, sometimes called the Viterbi algorithm, to solve the optimization problem. Dynamic programming is a global, non-iterative optimization strategy that finds the shortest path through transitioning states given a cost to go from one state to the next set of states. In the context of block-matching motion tracking, each state represents the displacement of a kernel. The next set of states is the displacement of the next kernel along an A-line. The transition cost is the chosen cost function that has a similarity and a continuity term. In Jiang and Hall's paper, normalized cross correlation was used as a similarity metric and a number of continuity terms were examined [30],

$$S = \sqrt{\left(\frac{\delta \vec{u}}{\delta x}\right)^2 + \left(\frac{\delta \vec{u}}{\delta y}\right)^2}$$

$$E_{c,a} = \frac{S}{\sqrt{|S|^2 + \beta}}$$

$$E_{c,b} = \begin{cases} e^S - 1, & S < 2 \\ \frac{S}{\sqrt{|S|^2 + \beta}} + e^2 - 1, & S \geq 2 \end{cases}$$

$$E_{c,c} = 2\left(e^S - 1\right)$$

Eqn. 3.3

In Rivaz's article, he examined the sum of absolute differences as a similarity metric and the following continuity term [31],

$$E_c = (d_i - d_{i-1})^2$$

Eqn. 3.4

where d_i is the displacement at sample *i*.

Brusseau used a sequential quadratic programming strategy to solve the optimization problem. This is a Newton like optimization technique that allows for constrained parameters. She applied normalized cross correlation as the similarity metric and used the following expression as a continuity term [5],

$$E_c = \left(\frac{\alpha - \alpha_{average}}{\alpha_{max} - \alpha_{min}} \right)^2 + \left(\frac{u - u_{average}}{u_{max} - u_{min}} \right)^2$$

Eqn. 3.5

Where α is a scaling factor related to the local strain and u is the local displacement.

3.3 Recursive Bayesian regularization

We will examine a regularization approach that attempts to optimize the displacement using both the block similarity metric and the motion of neighboring blocks. However, unlike the aforementioned algorithms, we do not explicitly formulate the problem as the minimization of a cost function. Instead, we follow the approach proposed by Hayton et al. [32] where the similarity metric is viewed in a probabilistic framework. Iterative Bayesian regularization is applied based on the similarity metric observed in neighboring blocks. Hayton et al.[32] originally applied this method for deformable image registration of magnetic resonance (MR) images obtained during breast imaging. The purpose of the algorithm was to register MR breast images taken before and after injection of a contrast agent, Gd-DTPA. Without registration, patient motion artifacts due to breathing and other motion would interfere with effective analysis of the images. A mutual information similarity metric was used in a multi-scale implementation. After the block-matching displacement estimates were obtained, they were used as initial values for a deformable cubic B-spline motion model that was regularized by a smoothing term, described as:

$$\rho \int \int u_{xx}^2 + 2u_{xy}^2 + u_{yy}^2$$

Eqn. 3.6

Finally, and optimization was performed with the conjugate gradient descent method.

The paper by Hayton has been referenced many times in the literature, but the author has not found a paper that has reimplemented the algorithm. However, another paper that describes application of the algorithm to an ultrasound registration case was published from the same Michael Brady Oxford University group. Xiao et al. [33] applied this method to the registration of 3D B-mode ultrasound subvolumes. B-mode breast ultrasound volumes were collected using a free-hand sweep of the region to be scanned using a 2D ultrasound transducer. Multiple sweeps are collected to obtain a larger area and reduce speckle noise through spatial compounding. Differing sweep speeds, angles, and tissue deformation require deformable registration of the sub-volumes. In contrast to the Hayton et al. [32] MR paper, normalized cross correlation was used as a similarity metric and single-level searching was performed. Like the Hayton et al. [32] experiment, the resulting displacements were input into a cubic B-spline parameter optimization with a smoothing term consisting of squares of the second derivatives of displacement and solved with the conjugate gradient descent method.

3.3.1 Algorithm

In block-matching methods, a small kernel from the pre-deformation image is compared to the post-deformation image using a similarity metric [34, 35]. We assume the comparison is made on a regular grid of points by translating the kernel within a specified search region. The grid of similarity metric values located at the kernel's center define a similarity metric image

associated with the kernel utilized for displacement estimation. Examples of similarity metrics include sum of absolute difference, sum of squared differences, normalized cross correlation, phase correlation, or mutual information [1, 2].

We can treat the similarity metric image as a probability image for the displacement of the kernel by applying a few basic transformations. First, the similarity must be inverted, if necessary, such that the maximum value corresponds the region with the greatest similarity. For normalized cross correlation or mutual information this is not required, but it is required for most other similarity metrics. Next, the metric must be shifted by the negative of the metric's theoretical minimum so the smallest resulting value is zero. In the case of normalized cross correlation, 1.0 is added to the similarity metric since its bounds are $[-1, 1]$. In the case of an inverted sum of squared differences, the theoretical minimum is negative infinity, but real world limited bit depth integer data and with finite signal length allow the use of a reasonable finite lower bound. Finally, the similarity metric values are normalized by their sum such that integral of all values is unity. The similarity metric image can now be treated as a probability image for displacement estimation using the kernel. A value of zero in the probability image occurs at the metric's theoretical minimum with the sum of probabilities being unity.

The probability images obtained are prior probability estimates, $Pr(\mathbf{u_x})$, in a Bayesian framework.

$$Pr(\mathbf{u_x}|\mathbf{u}_{\mathcal{N}_x}) = \frac{Pr(\mathbf{u}_{\mathcal{N}_x}|\mathbf{u_x})Pr(\mathbf{u_x})}{Pr(\mathbf{u}_{\mathcal{N}_x})}$$

Eqn. 3.7

where $\mathbf{u_x}$ is the displacement of the kernel at location $\mathbf{x}$ and $\mathbf{u}_{\mathcal{N}_x}$ is the displacement at the neighboring kernels. The denominator, $Pr(\mathbf{u}_{\mathcal{N}_x})$ serves at as a normalizing constant. This factor is accounted for by re-normalization at the end of each iteration of the algorithm.

We assume that $Pr(\mathbf{u}_{\mathcal{N}_x}|\mathbf{u_x})$ can be modeled by the probabilities of the displacements estimated at immediate neighbors, i.e. four neighbors in 2D. In addition, we assume that these probabilities are independent.

$$Pr(\mathbf{u}_{\mathcal{N}_x}|\mathbf{u_x}) = \prod_{\mathbf{x'} \in \mathcal{N}_x} Pr(\mathbf{u_{x'}}|\mathbf{u_x})$$

Eqn. 3.8

Here $Pr(\mathbf{u_{x'}}|\mathbf{u_x})$ is the probability that a neighboring block at $\mathbf{x'}$ has a displacement $\mathbf{u_{x'}}$ given a displacement $\mathbf{u_x}$ at $\mathbf{x}$. The assumption of independence is usually invalid, but iterative application of the algorithm is intended to account for some of the expected correlation between neighboring displacement estimates.

We model $P(\mathbf{u_{x'}}|\mathbf{u_x})$ as the maximum of the neighboring probability image modulated by a Gaussian term.

$$Pr(\mathbf{u_{x'}}|\mathbf{u_x}) = \max_{\mathbf{v}} \left[Pr(\mathbf{v_{x'}}) \exp(\frac{-||\mathbf{v_{x'}} - \mathbf{u_x}||^2}{2\sigma_{\mathbf{u}}{}^2}) \right]$$

Eqn. 3.9

Here $\mathbf{v_{x'}}$ is the displacement at $\mathbf{x'}$. We restrict the above to $||\mathbf{v_{x'}} - \mathbf{u}|| < \epsilon$, where ϵ is a threshold. The $\sigma_{\mathbf{u}}$: is a vector that determines the width of Gaussian-like term for each

direction. If δ_x is the spacing between kernels in one direction, then $\sigma_\varepsilon = \sigma_u/\delta_x$, the strain regulation sigma (SRS), represents the algorithm's parameter in terms of a factor related to the expected strain. Spacing between kernels can be decreased by increasing kernel overlap or decreasing their dimension.

A likelihood term for the Bayesian model can then be written as,

$$Pr(\mathbf{u}_{\mathcal{N}_x}|\mathbf{u}_\mathbf{x}) = \prod_{\mathbf{x}'\in\mathcal{N}_x} Pr(\mathbf{u}_{\mathbf{x}'}|\mathbf{u}_\mathbf{x}) = \prod_{\mathbf{x}'\in\mathcal{N}_x} \max_\mathbf{v} \left[Pr(\mathbf{v}_{\mathbf{x}'})\exp(\frac{-||\mathbf{v}_{\mathbf{x}'} - \mathbf{u}||^2}{2\sigma_\mathbf{u}{}^2}) \right]$$

Eqn. 3.10

The influence of neighbors beyond adjacent blocks can be achieved by recursively applying the regularization.

The displacement of the kernel is taken according to the *maximum a posteriori* principle.

$$\mathbf{u}_\mathbf{x} = \arg\max_{\mathbf{u}_\mathbf{x}} Pr(\mathbf{u}_\mathbf{x}|\mathbf{u}_{\mathcal{N}_x})$$

Eqn. 3.11

Subsample precision of the displacement is achieved using interpolation of the posterior probability.

3.3.2 Implementation

A multi-threaded version of the described algorithm was implemented with the Insight Toolkit [36] using normalized cross-correlation as the similarity metric for the results presented in this chapter.

The search region was 17 A-lines in the lateral direction along with sufficient data points along the axial direction to capture the maximum displacement for analysis. A simple unguided search was used, which is sufficient for the following analysis but not computationally efficient. The means to provide a computationally efficient implementation is achieved with the multi-resolution methods described in the other chapters. For a 2D image, the computational complexity scales with order $\mathcal{O}(n^2)$ for a search region of side length n. That is, the computational load quadruples as the size of the search region doubles. The size of the search region can be significantly reduced by using a coarse-to-fine or multi-scale approach. Motion estimates from sub-sampled images are used to initialize the center of the search region in finer resolution images.

The quantity ϵ, where $\|\mathbf{v}_{\mathbf{x}'} - \mathbf{u}\| < \epsilon$ was taken to be $3\sigma_u$.

We followed the recommendations described in [32] and [33] and applied the natural logarithm operator before the exponential operator after computing posterior probabilities. The idea is that additions, which are not as computationally expensive as multiplications, can be used in the convolution-like operation used for computing posterior probabilities. That is, the log posterior probability is computed using

$$Pr_{log}(\mathbf{u}_{\mathbf{x}}|\mathbf{u}_{\mathcal{N}_x}) \propto \sum_{\mathbf{x}' \in \mathcal{N}_x} \max_{\mathbf{v}} \left[Pr_{log}(\mathbf{v}_{\mathbf{x}'}) - \frac{\|\mathbf{v}_{\mathbf{x}'} - \mathbf{u}\|^2}{2\sigma_{\mathbf{u}}^2} \right] + Pr_{log}(\mathbf{u}_{\mathbf{x}})$$

Eqn. 3.12

The statement is only proportional because it does not contain the denominator in Bayes' Theorem, which is accounted for by re-normalization after taking the exponential of the posterior probability.

3.4   Experimental methods and results

3.4.1   Uniform strain simulations and phantoms

A uniform elastic modulus tissue-mimicking (TM) ultrasound phantom was tested. Frames

of data were continuously collected as the unconstrained phantom was deformed with an acrylic

plate. The plate was fitted with a transducer at the center and translated using a linear motion

table. The phantom was scanned using a Siemens S2000 (Siemens Ultrasound, Mountain View,

CA, USA) clinical ultrasound system equipped with a VFX9-4 transducer and the plane through

the center of the sphere imaged. The transducer was excited at 8.9 MHz and RF data was

sampled at 40 MHz to a depth of 5.5 cm.

Twenty independent deformation experiments were performed by varying the pre-

deformation frame index within the continuous loop to obtain statistically significant results.

The frame average strain was controlled by the frame skip between pre-deformation and post-

deformation frames.

Displacement estimation error was quantified using the elastographic signal-to-noise (*SNRe*)

ratio computed along the axial direction [35]

$$SNR_e[dB] = 20\log 10\left(\frac{m_\varepsilon}{s_\varepsilon}\right)$$

Eqn. 3.13

where m_ϵ and s_ϵ are the mean and standard deviation of the axial strain, respectively.

Calculation of the *SNRe* was restricted to the area around the transducer's focus.

Numerical ultrasound simulations were designed to mimic the ultrasound physics and solid

body mechanics present in the phantom. The simulated RF data was generated using an ultrasound frequency domain simulation program developed in our laboratory [37]. Uniformly distributed and randomly positioned acoustic scatterers were generated and their response to a linear array transducer over a range of frequencies calculated. A particular ultrasound transducer was simulated by multiplying the phantom response in the frequency domain with the spectrum for the ultrasound transducer of interest. A single row of 128 elements was the aperture, with a spacing of 0.2 mm between elements. An individual element had a size of 0.15 mm laterally and 10 mm in the elevational direction. The beamspacing was 0.2 mm, and the transmit focus was located at a depth of 20 mm. This yielded the Fourier Transform of the RF data of interest. For these experiments, the simulated transducer's spectrum was modeled as Gaussian with a center frequency of 8.0 MHz and a 40% fractional bandwidth. The simulated transducer array had a channel count of 128 elements. Displacements were applied to the individual scatterers that made up each numerical phantom, to produce a set of post-deformation numerical phantoms and the accompanying RF data. A 40mm×40mm×10mm volume of scatterers was simulated.

The axial displacement field for a uniform elastic modulus phantom undergoing unconstrained compression along the axial direction is simply a linear increase in displacement starting from zero at the transducer surface. The slope of the displacement is the amount of strain applied. In the lateral direction the displacement often starts from zero at the center of the phantom and increases linearly towards the edge of the phantom. The slope of the displacement is the applied axial strain multiplied by Poisson's ratio. If we assume an incompressible material as is common for soft tissues and the gelatin phantoms, the Poisson's ratio is near 0.5.

Deformation estimation statistics on n=30 randomly generated collections of scatterers were collected.

The simulations of a uniformly elastic TM block were examined in a manner similar to the uniform TM phantom and evaluated for variations in the SNRe with applied deformation. In order to visualize the effectiveness of recursive Bayesian regularization, we quantified errors at 0.5%, 1.0%, 3.0%, 5.0%, 7.0%, and 9.0% strain in the TM phantom and numerical simulation images. Tracking kernel size used was 41 points (0.8 mm) in the axial direction and 9 points (1.1 mm) in the lateral direction. Error bars denote two standard errors of the error measures corrected for repeated measure means [38].
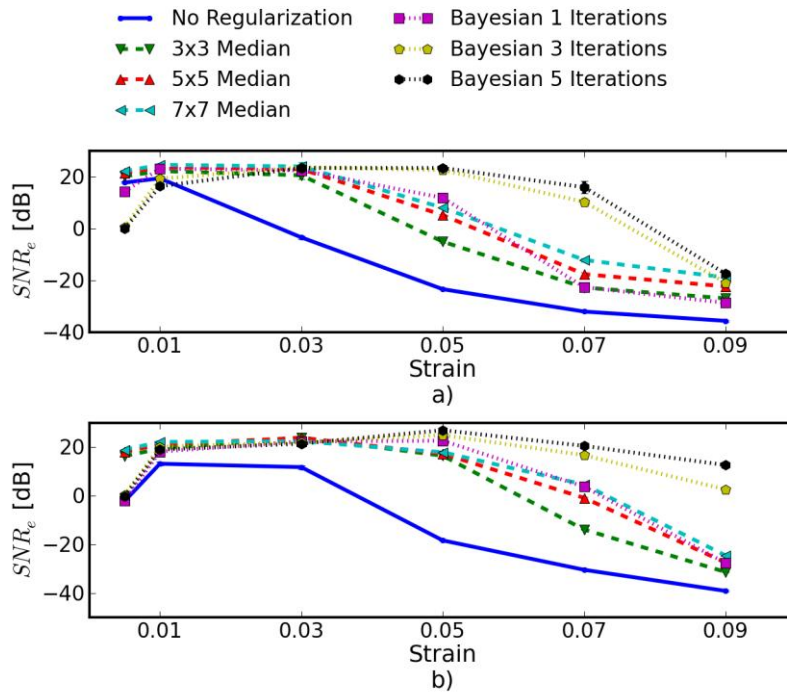
Figure 3.1: Motion tracking quality (SNRe) versus applied strain for a) uniform phantom and b) uniform simulation.

In Fig. 3.1 we observe that, especially for high strains, Bayesian regularization outperforms median filtering or no regularization. The same bandpass type pattern [39] is seen for both the phantom and simulation. With regularization, the simulation performs better at the highest

strain, 9.0%. This may be explained by the deformation model used in the simulation: the simulation does not have out-of-plane motion, which may occur at high strains and causes large signal decorrelation. Note that for very low strains, 0.5%, the Bayesian regularization causes a regression in performance.

3.4.2 Circular inclusion simulations and phantoms

A TM ultrasound elastography phantom subject to uniform deformation was imaged using a clinical ultrasound scanner. The $10\times10\times10$ cm gelatin phantom had a 1.0 cm spherical inclusion near its center. This type of phantom is common in the elastography literature because of its simple, well known behavior and resemblance to an isolated tumor within background tissue.

Displacement estimation error for comparison with the median filter and optimization of strain-regularization-sigma (SRS) was computed as follows. The estimated displacements were interpolated with cubic B-spline interpolation such that the sampling of the displacement image matched that of the RF data. The inverse displacement was applied to each pixel in the pre-deformation image, and windowed-sinc interpolation applied to find the corresponding RF value in the post-deformation image. A mean absolute RF difference (MARD) is reported excluding the edges of the image where edge effects or out-of-bounds conditions may occur.

$$MARD = \frac{\sum_{i=1}^{n} |I_m(\mathbf{x}_i - \mathbf{u}_{x,i}) - I_f(\mathbf{x}_i)|}{n}$$

Eqn. 3.14

where I_m is the interpolated RF value in the post-deformation (moving) image and I_f is the RF value in pre-deformation (fixed) image.

In order to simulate the circular inclusion, displacement fields were generated by specifying the mechanical properties of interest, and applying uniform displacements as boundary conditions using commercially available finite element software, ANSYS (ANSYS Inc, Pittsburgh, PA, USA). Displacement fields were generated for a simulation having a uniform background modulus of 2kPa and a circular inclusion with a modulus of 8 kPa. The inclusion's diameter was 8 mm. Boundary conditions were as follows. Uniform displacements were applied across the top surface of each simulated phantom along the axial direction such that the nominal strain produced in the simulation was equal to 0.5%, 1.0%, 3.0%, 5.0%, 7.0%, and 9.0%. The bottom surface of the simulated phantom was constrained to have no axial displacement, and a single node was fixed in the lateral direction at the bottom, to ensure uniqueness of the solution. Displacement fields from a nearly incompressible (Poisson's ratio of 0.495) material modeled in a plane stress state were simulated and applied to the numerical phantoms. The mechanical model represents a cylindrical inclusion in an unconstrained background, which is similar in its deformation to the spherical inclusion phantom [40].

Again, deformation estimation statistics on n=30 randomly generated collections of scatterers were collected. Displacement estimation error for comparison with the median filter and optimization of SRS were computed as follows. Output displacements from the finite element simulation were interpolated with cubic B-spline interpolation at locations where displacement estimation occurred. A mean absolute axial displacement difference (MADD) is reported excluding the edges of the image, where edge effects may occur.

$$MADD = \frac{\sum_{i=1}^{n} |\hat{u}_a - u_a|}{n}$$

Eqn. 3.15

where $\hat{u}_a$ is the estimated axial displacement and u_a is the known axial displacement.

We present estimated axial strain images with and without regularization at a 5.0% applied deformation. We also generated strain images after filtering the displacements with a 3×3, 5×5, and 7×7 pixel median filter for comparison.
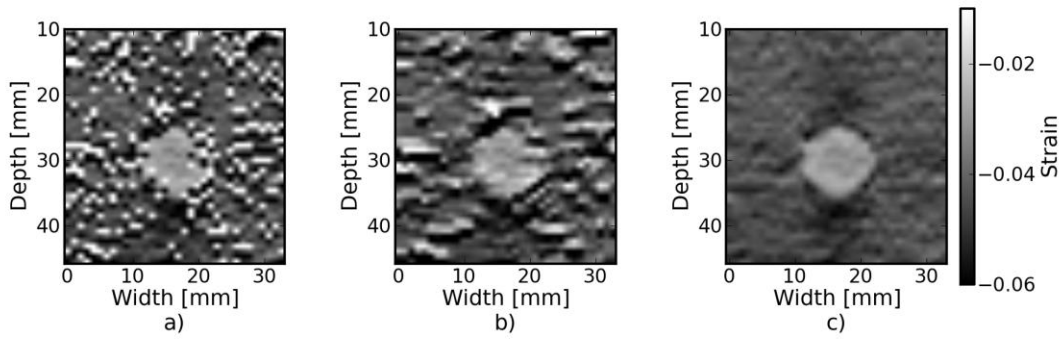

Figure 3.2: Phantom axial strain images with different types of regularization applied. a) No regularization. b) 3×3 median filter applied to the displacements. c) Three iterations of the proposed regularization algorithm.
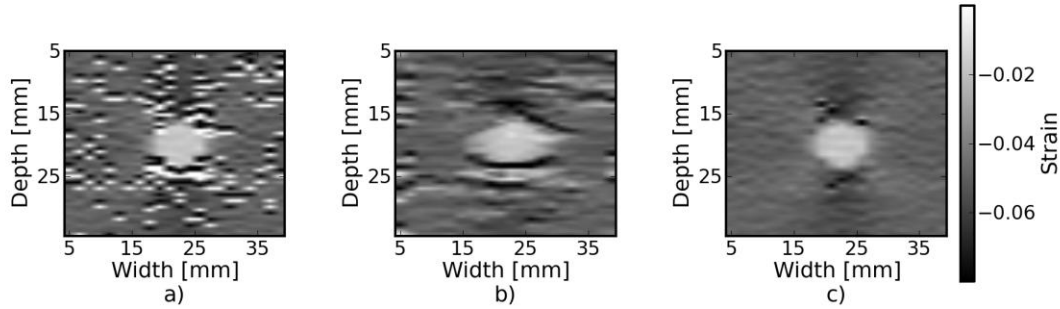
Figure 3.3: Simulation axial strain images with different types of regularization applied. a) No regularization. b) 3×3 median filter applied to the displacements. c) Three iterations of the proposed regularization algorithm.

Examples of the algorithm's effectiveness are shown in Fig. 3.2, and Fig. 3.3. Figure 3.2 shows axial strain images of the phantom data with no regularization (a), median filtering of the displacements (b), and recursive Bayesian regularization (c). With no regularization, there are considerable peak hopping errors limiting the ability of median filtering to remove these errors. Instead, these errors are 'smeared', which arguably makes the regularized image worse than the original because the peak hopping errors are more likely to be interpreted as artifactual tissue structures. The proposed Bayesian regularization on the other hand, does an excellent job of removing these noise artifacts from the image. Results are similar for the numerical simulation results, shown in the Fig. 3.3. Again, considerable signal decorrelation noise is present in the uncorrected image. Median filtering removes a good portion of the noise, but it also results in a noticeable loss of resolution at the boundary of the inclusion. The Bayesian regularization does a better job of removing noise while increasing the observable strain pattern surrounding the inclusion. However, a few peak hopping errors are not removed as illustrated in Fig. 3.3(c).
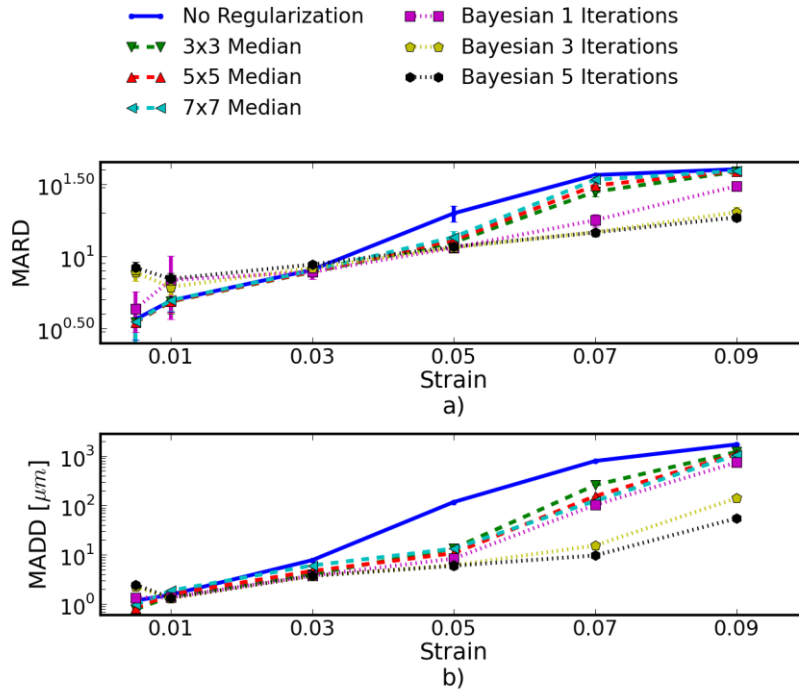
Figure 3.4: Motion tracking quality versus applied strain for a) spherical inclusion phantom and b) cylindrical inclusion phantom simulation. Different quality metrics are applied to the appropriate experiment-- a) uses mean absolute RF phantom image RF difference (MARD) versus regularization method (lower is better) and b) uses mean absolute displacement difference between the simulated and estimated displacements (lower is better).

Quantification of the results observed visually in Fig. 3.2, are shown in Fig. 3.4(a) and the corresponding simulation results indicated visually in Fig. 3.3 are plotted in Fig. 3.4(b). Mean error metrics for the inclusion experiments are plotted against strain for each regularization method. Error bars again denote two standard errors of the error measures corrected for repeated measure means [38]. Results are consistent across strain content, simulation and phantom data, and methods for measuring the tracking quality of the estimated displacement. Bayesian regularization greatly improves motion tracking performance over no regularization and median filtering at large strains, 5.0% and higher. Improvement is on par with median filtering at

moderate strains, 3.0%. For small strains, <1.0%, Bayesian regularization may decrease performance relative to no regularization. In general, increased iterations of the proposed algorithm results in greater improvement, but the relative improvement from three iterations to five iterations is much smaller than one iteration to three iterations. In contrast, the ideal median filter size varies depending on the strain content and the amount of applied deformation. This is consistent with our visual observations of the algorithm's behavior; images improve up to approximately three iterations after which the improvement is not as noticeable.

3.4.3 Optimal SRS

An optimal SRS under different conditions was extracted by minimizing the described error measure for both TM phantom and numerical simulation images. Brent's method for scalar minimization [41] was performed to a tolerance of 0.001. The optimal SRS was examined over a range of strains, kernel overlaps, and algorithm iterations. Unless otherwise noted, strain examined was 5%, kernel separation was 0%, and the number of iterations was set to three. Although SRS can be specified independently in all directions, SRS reported is the parameter's value along the axial direction. The value in the lateral direction was taken to be half the value in the axial direction since unconstrained compression of nearly incompressible elastic materials lead to strains in orthogonal planes that are half that along the loading axis, i.e. the incompressibility assumption. Note, however, the parameters for each direction can be specified independently, and strain in one direction does not directly influence strain in the other directions.
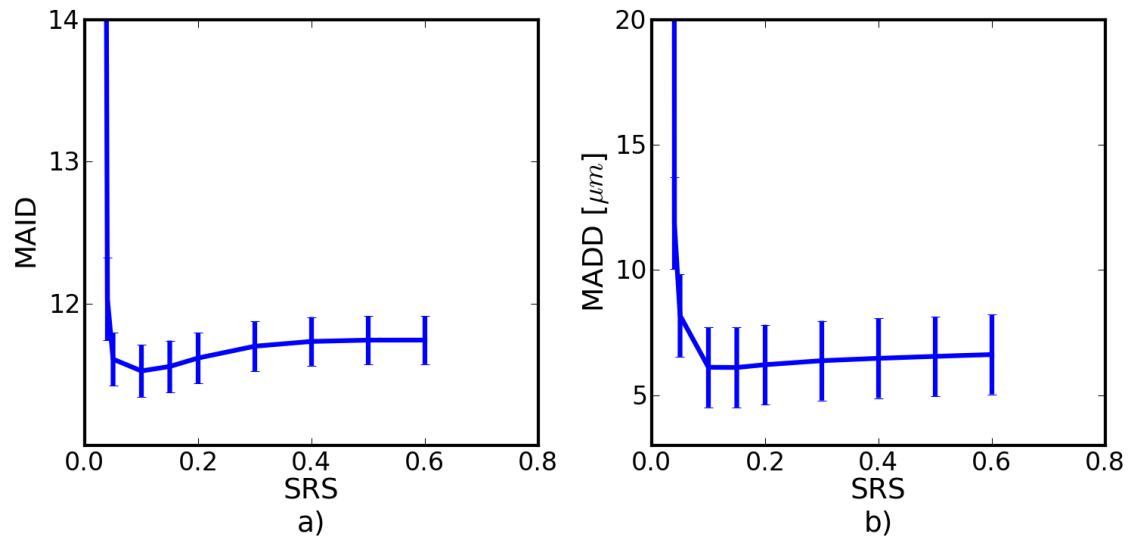
Figure 3.5. Error measures on a) phantom and b) simulation versus the regularization parameter. The nominal strain in both cases was 5 %.
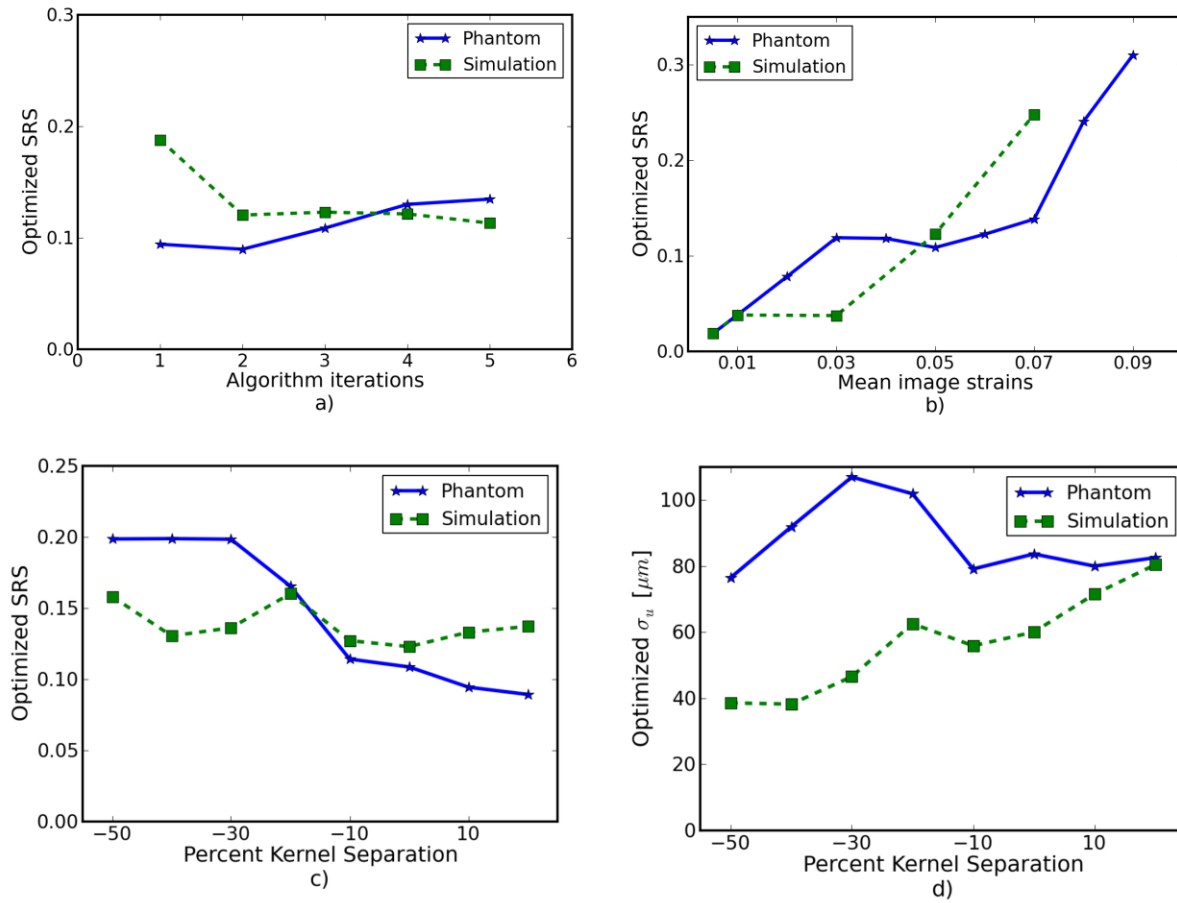
Figure 3.6: Variation in the optimized regularization parameter with a) the number of algorithm iterations, b) image strain, and c) block matching kernel overlap. To contrast with c) the optimized regularization parameter multiplied by block matching kernel spacing versus block matching kernel overlap is shown in d).

Figure 3.6(a) shows optimized SRS versus the number of algorithm iterations. No consistent pattern is observed. This suggests the optimization parameters do not strongly depend on the number of iterations. As expected, Fig. 3.6(b) demonstrates that the optimal SRS increases with increasing image strain. The optimal parameter is approximately twice the image strain. A decrease in SRS is seen in Fig. 3.6(c) with phantom images, but a consistent trend is absent from the simulation images. The deviation in optimized parameters in either case is

relatively small given the flatness of the error metric shown in Fig. 3.5. Figure 3.6(d), which plots σ_u as opposed to SRS, is shown to contrast with Fig. 3.6(c). Phantom images again demonstrate a downward trend while simulation images suggest an upward trend. Optimized parameters for phantom images and simulation images are more consistent in Fig. 3.6(c) than Fig. 3.6(d), which suggest SRS may be a more consistent parameter than σ_u.

3.4.4 Addressing carotid reverberations

While the Bayesian regularization is effective at removing signal decorrelation noise, it is also effective at removing reverberation artifacts. Reverberation artifacts are a source of noise in both B-mode and estimated strain images. A reverberation is a received signal that is the result of multiple scattering events. The time delay and apparent depth of a reverberation artifact is longer and deeper than the true source of the original backscatter event. The motion of a reverberation artifact is not necessarily congruent with backscattered signal from local tissue. In fact, the displacement of the reverberation may be in the opposite direction of the local tissue. If the reverberation signal is stronger than the local tissue inside the matching kernel, an artifactual displacement estimate will be generated. However, if we use a regularization method that incorporates displacement estimates from surrounding matching kernels, the artifact can be removed. In this section we demonstrate the removal of a carotid reverberation and illustrate the algorithm's behavior during each iteration.

The following images show the area of focus in the longitudinal carotid B-mode taken with the 18L6 on a Siemen's S2000 clinical ultrasound system. The imaging plane bisects the common carotid artery throughout almost the entire image. On the left the carotid bulb begins, with a thick plaque region originating at its base. Observation of a B-mode video clip of the region clearly elucidates the high intensity reverberation located in the center of the matching

kernel. The reverberation's motion, upward, is opposite to the motion of the vessel wall, downward.
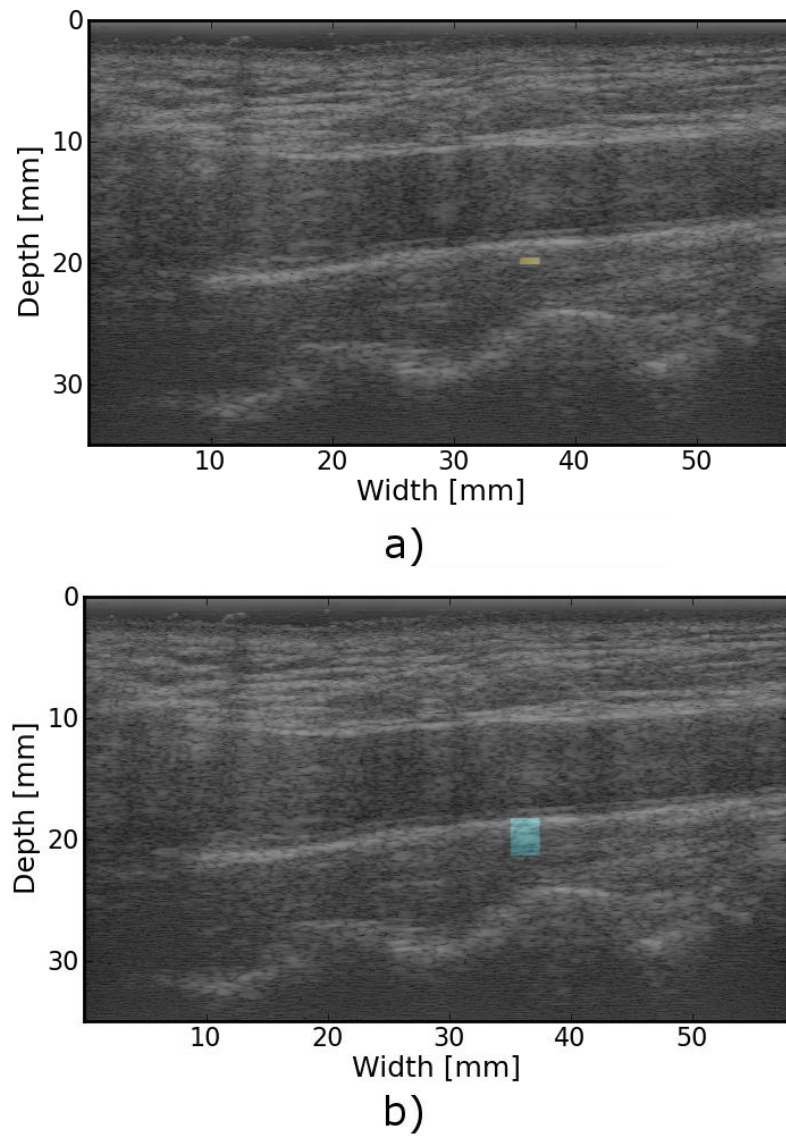

Figure 3.7: a) Longitudinal common carotid artery (CCA) B-mode with highlighted locations of the matching kernel (yellow), and b) the search region (cyan) that are subsequently analyzed in fine detail.

Focusing on the area of interest, we next examine initial probability image for the
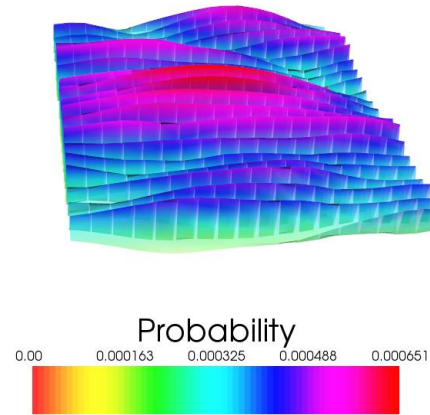
displacement of the kernel.

Figure 3.8: Probability image for the matching kernel's displacement.

Each point in the probability image is created by using normalized cross correlation to compare the RF data in the matching kernel from the pre-deformation image to the RF data in the post-deformation image. The result is shifted by negative one, the theoretical lower bound, and normalized such that the sum of the values add up to one. This is the prior probability for the displacement of the matching kernel before the algorithm has been applied. The peak, the red region, is where the displacement would be estimated. We see that the ultrasound's point response function affects the probability image; the image has rapid oscillations along the axial direction and slowly developing peaks with relatively low definition in the lateral direction.
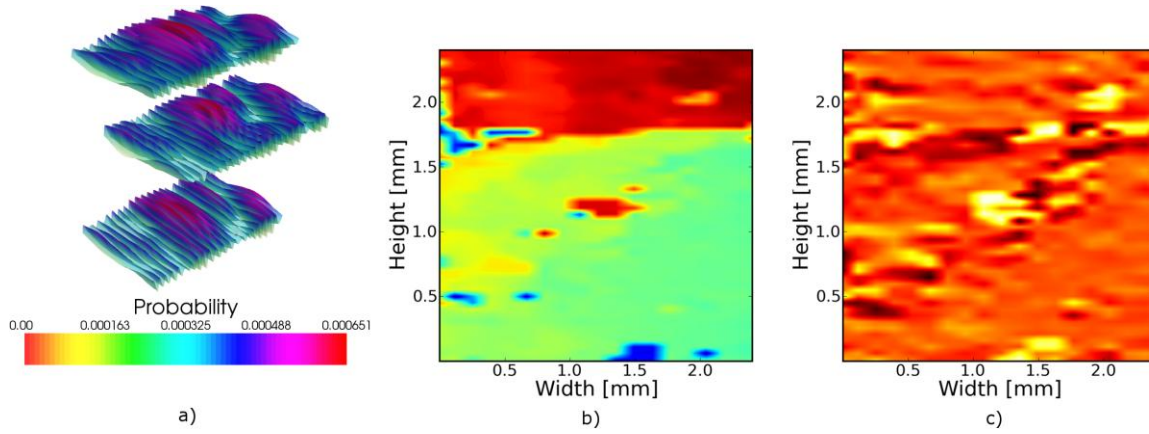
Figure 3.9: a) Probability images, b) axial displacement image in the ROI, and c) axial strain image in the ROI for iteration 0 (no regularization).
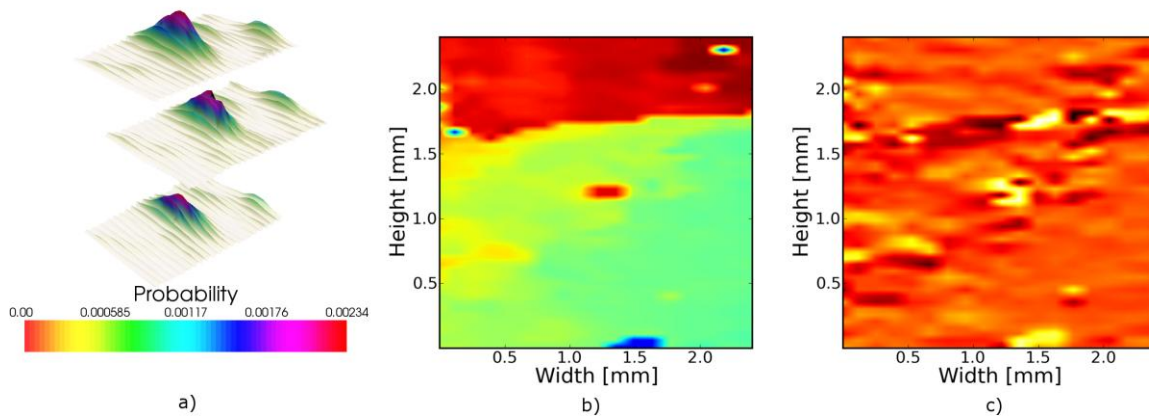

Figure 3.10: a) Probability images, b) axial displacement image in the ROI, and c) axial strain image in the ROI for iteration 1.
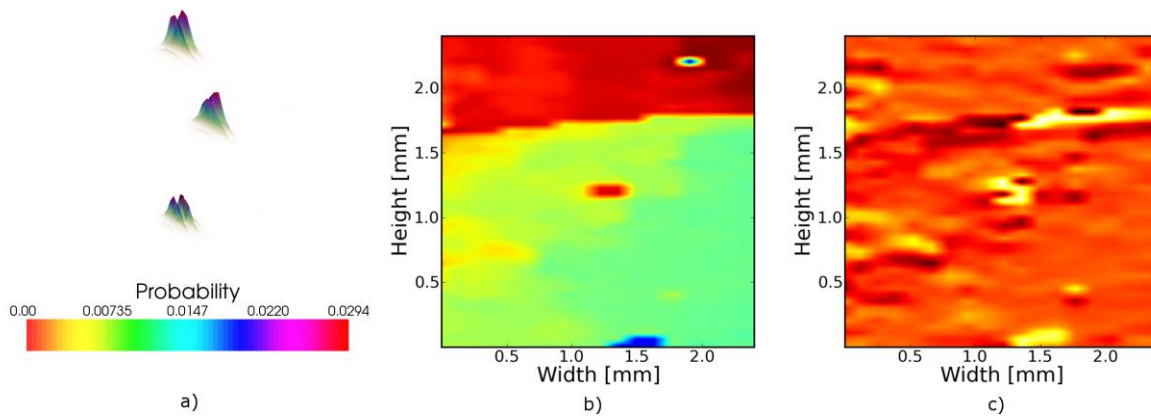
Figure 3.11. a) Probability images, b) axial displacement image in the ROI, and c) axial strain image in the ROI for iteration 2.
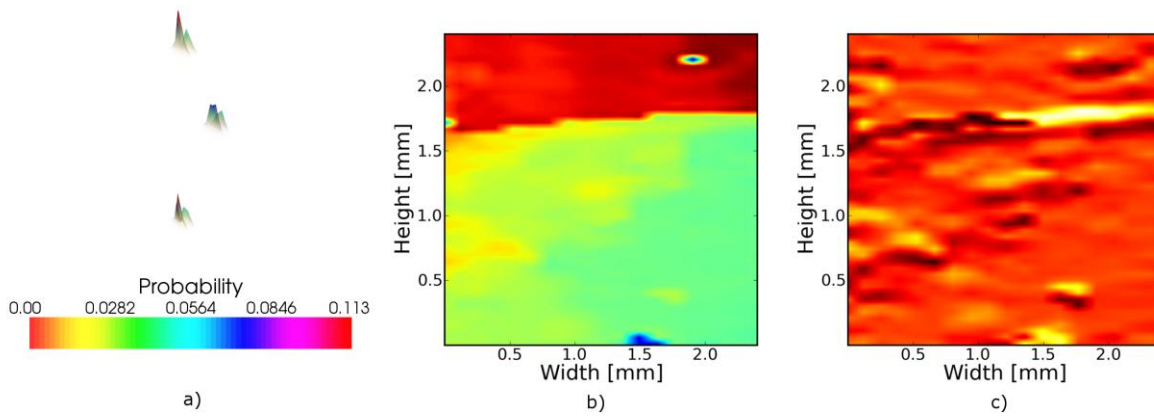

Figure 3.12. a) Probability images, b) axial displacement image in the ROI, and c) axial strain image in the ROI for iteration 3.

In Fig. 3.9 to Fig. 3.12 we examine the evolution of our region of interest (ROI) from no regularization (iteration zero) to three iterations of our recursive Bayesian algorithm. The probability images of our matching kernel of interest (top), a lateral neighbor (middle), and an axial neighbor (bottom) display algorithm performance at specific points while the axial displacement and strain images display the general situation in the region.

Structures present in the B-Mode image can be identified in Fig. 3.9. Near the top of Fig.

3.9b) we see the change in displacement that occurs at the vessel wall. High strain in the vessel wall can be observed in Fig. 3.9c). In both Fig. 3.9b) and Fig. 3.9c) tracking of the reverberation's discontinuous motion can be observed in the center of the image. Without regularization, the peaks in Fig. 3.9a) are not distinctive. We also note the extent of the noise in the displacement and strain image.

After the first iteration, the posterior probability densities shown in Fig. 3.10a) concentrate their energy in the same confined region in all three probability images. The noise is reduced in Fig. 3.10b) and Fig. 3.10c), but the reverberation artifact is still present.

Not that at the second iteration, as shown in Fig. 3.11, it is easily visible that all three of our probability images are bimodal. One mode corresponds to the displacement of reverberation while the other mode corresponds to the displacement of the local tissue. However, the reverbation peak is still stronger as the artifact is still observable in Fig. 3.11b) and Fig. 3.11c).

Finally, after the third iteration, the local tissue mode dominates in Fig. 3.12a) causing the reverberation artifact to be removed from Fig. 3.12b) and Fig. 3.12c).
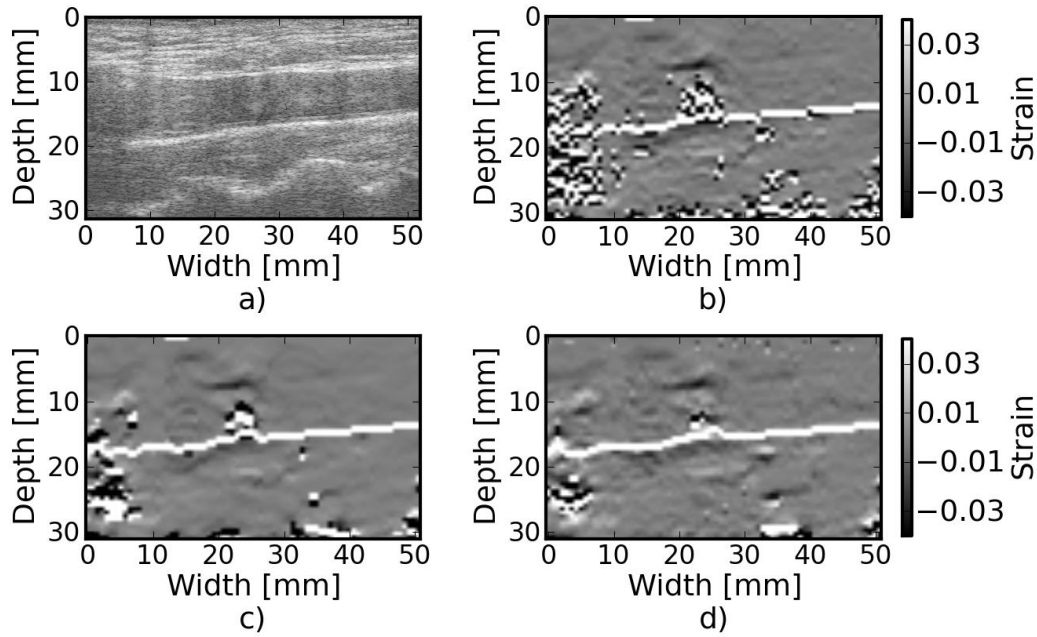
Figure 3.13: Strain images of an atherosclerotic carotid bulb during systole. a) B-Mode. b) No regularization. c) 3×3 median filter applied to the displacements. d) Three iterations of the proposed regularization algorithm.

Figure 3.13 shows an atherosclerotic artery undergoing compression during systole. Bayesian regularization removes many of the peak hopping artifacts in the areas of high strain, roughly 3% and higher. However, note that in areas distant from the vessel wall, where there is little to no deformation, Bayesian regularization introduces additional artifacts compared to the case with no regularizations. This may be expected given the poor performance at very low strains that is observed in Fig. 3.1 and Fig. 3.4. The MARD was 55.6, 50.5, and 46.6 for no correction, median filtering, and Bayesian regularization, respectively.

3.4.5   Improvement of a liver ablation

In order to examine the performance in another clinical application, we visualize strain images from porcine liver. The images correspond to a radiofrequency ablation performed on an

open-abdominal *in vivo* porcine model with a healthy liver. The study was approved by the research animal care use committee of the University of Wisconsin-Madison. Details about this study are presented in [42]. The source of deformation in this case was movement of the ablation electrode and breathing of the animal. This case used the Siemens 9L4 linear array transducer.

Liver and carotid B-mode images are displayed along with axial strain images with no regularization, 3×3 median filtering, and three iterations of Bayesian regularization. As with the spherical inclusion phantom, MARD is calculated to quantify the quality of motion tracking.
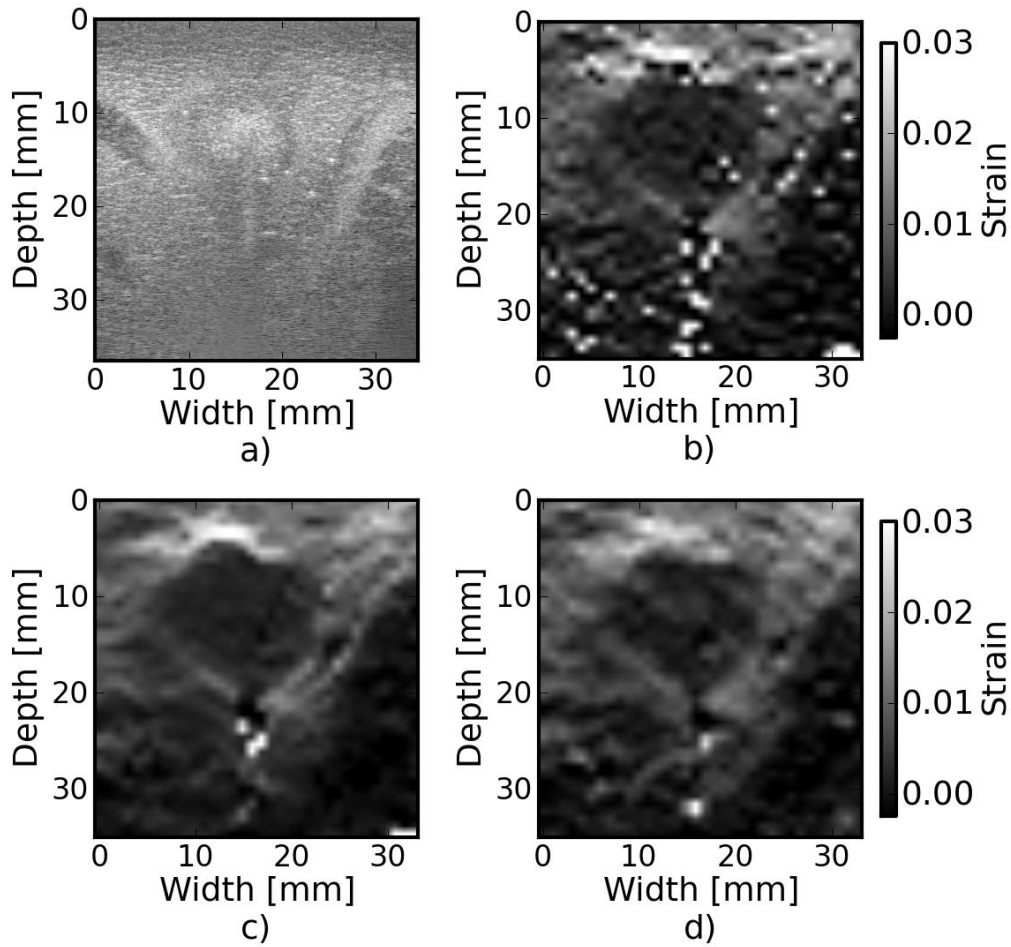
Figure 3.14: Strain images from a liver undergoing RF electrode ablation. a) B-Mode. b) No regularization. c) 3×3 median filter applied to the displacements. d) Three iterations of the proposed regularization algorithm.

Results from tracking tissue RF echo signals for the ablated region are shown in Fig. 3.14. The ablated liver tissue observable in Fig. 3.14(a) causes the reduced strain region in the strain images. Both median filtering and Bayesian regularization remove the majority of peak hopping errors. The median filtered image appears smoother while the Bayesian regularization image has more detail, although the true underlying strain is unknown, so it is difficult to associate a correct

image from appearance. Bayesian regularization does slightly better at handling shadowing from the electrode ablation needle at the bottom of the ablated region. The MARD values were 150.0, 127.6, and 124.1 for no regularization, median filtering, and Bayesian regularization, respectively.

3.5 Discussion

Block matching based displacement tracking methods can regularize the estimated displacement to reduce noise artifacts by enforcing the diffeomorphic transformation expected in images of solid tissue. Filtering methods such as median filtering take into account displacements of neighboring tracking kernels and can reduce noise artifacts, but come at the cost of spatial resolution. Better regularization performance is possible when incorporating similarity metric values from neighboring blocks prior to displacement estimation.

The method described in this chapter is analogous to regularization algorithms that minimize a cost function involving a similarity metric and a continuity metric [31, 30, 23]. However, transforming the similarity metric image into a probability distribution allows use of the similarity metric's weight in determining displacements to vary dynamically depending on the local uncertainty. The weight of the similarity metric does not depend on its absolute value. Instead, weight of the similarity metric is adjusted locally to the noise conditions in a tracking kernel's search region. This independence of local or global noise improves robustness of the local estimated displacements.

Due to its statistical nature, the algorithm encourages a continuous solution, but it still allows discontinuous motion when it is strongly suggested by the data. This is important for Fig. 3.13, where opposing arterial walls move in opposite directions.

The form of the likelihood term in the Bayesian model suggests that a Gaussian distribution in the estimated strain is expected since it involves the difference in displacements and kernel spacing is constant. The actual strain distribution depends on the modulus distribution and boundary conditions of the tissue imaged, but a Gaussian distribution is an appropriate generic form because of the Central Limit Theorem. As long as the regularization parameter is large enough, the algorithm performs across a wide range of strains. This robustness can be inferred from the flatness in the latter portion of Fig. 3.5. If the variance of the Gaussian is presumed to be too small, large strains are not possible, and regularization will degrade the quality of motion tracking. Furthermore, we have shown that the parameter does not have to be chosen arbitrarily because of its meaningful interpretation in terms of the expected strain. In Hayton's original article, he remarked on the complex interaction of the Gaussian likelihood standard deviation with kernel spacing [32]. The term σ_u controls the probability of δu in $\delta u / \delta x$ but the kernel spacing scales δx in $\delta u / \delta x$. When we formulate σ_ε as $\sigma_u / \delta x$ the algorithm's parameters are decoupled into a single parameter with a meaningful interpretation. A good SRS can be determined analytically as opposed to heuristically with a rough knowledge of the expected strain. Figure 3.6(b) shows that the optimal parameter increases with the image strain. However, the relationship is not expected to be strictly linear. A strain image will contain a distribution of strain amplitudes, and signal decorrelation also varies with the applied strain [39], which will also affect the optimal parameter. In an approximate sense, the SRS can be viewed as the standard deviation of a function that modulates the estimated strain.

As seen in Fig. 3.1 and Fig. 3.4, Bayesian regularization can greatly increase the quality of motion tracking and dynamic range of strains that can be imaged. This improvement is mostly seen at higher applied deformations, i.e. 5% and larger. For very small strains, application of

the algorithm can decrease image quality compared to the case with no regularization. The source of noise at small strains is predominately electronic and quantization noise [39], and quantization noise may prevent the algorithm from being effective at these levels. This behavior along with the additional computational expense, suggest it may be desirable to limit application to high strain situations when applied in a clinical setting.

Various methods, given in the subplots of Fig. 3.1 and Fig. 3.4, were used to to validate the algorithm. The *SNRe* is a common method for evaluating strain imaging algorithms in the literature that characterizes the dynamic range and peak *SNRe* available [39]. Typically, an algorithm has difficulty at low strains and high strains, which gives the curve a 'bandpass filter' shape [39], observable in Fig. 3.1 and Fig. 3.4. The regularization greatly increases the dynamic range at the higher end, but slightly compresses it at the lower end. Since the *SNRe* is calculated on a uniform target, it does not demonstrate the ability of the algorithm to faithfully reproduce structures, which is often the purpose of creating the image. For this reason, we also evaluated performance with an inclusion target. For the simulation case, we have perfect knowledge of the true underlying displacement, so we can calculate the MADD. The MADD is a measure of the estimated displacement's fidelity over the entire image. In the phantom case, the true displacement is not precisely known, so the MARD error measurement is used. The MARD similarly measures the estimated displacement's fidelity if the motion of the RF signals can be assumed to follow the motion of the tissue from which it is generated. Since the shape of the MARD curves coincide well with the other error measures, its use in providing a quantitative assessment of the *in vivo* examples is justified. The *in vivo* examples demonstrate the algorithms effectiveness in more realistic clinical conditions.

Application of regularization of course comes at a computational expense. We have not

attempted a real-time implementation, but the following observations were made on the computational complexity. First, the algorithm is easily parallelizable and was implemented as a multi-threaded filter on a central-processing-unit (CPU). The shifting, normalization, and logarithm operations are all parallelizable. Computation of the likelihood term is parallelizable on a per displacement basis in a given iteration. Particular computational expense comes in the calculation of the likelihood term, which is a convolution-like operation. This has the following implications. Although Fig. 3.5 suggests a safe choice of SRS is higher, this will come at an additional computation expense because the Gaussian term becomes larger. Also, the size of the search region should be minimal to reduce calculation of the likelihood terms. Approaches such as a multi-resolution pyramid [24] where subsampled search regions that cover a large area of physical space are used to initialize smaller search regions may be helpful.

In the removal of a carotid reverberation case study, we showed that, unlike a median filter, the method is effective at removing reverberation artifacts. This is especially important for carotid strain images, where reverberations are abundant relative to tissues like liver. In the carotid low attenuation in the blood and a number of high strength, coherent reflectors at the muscles walls, artery wall, and blood-lumen interface contribute to a higher concentration of reverberations.

3.6 Summary

We propose the application of a recursive Bayesian regularization algorithm for carotid ultrasound strain imaging. This algorithm applies a probabilistic model to the similarity metric and imposes a Gaussian distribution on the estimated strain when incorporating the results of neighboring matching kernels. Results from *in vivo*, TM phantom and numerical simulations were presented, and the proposed algorithm performs better than median filtering of the

displacements. Application of this regularization is particularly appropriate for images of the carotid artery where reverberations are abundant.

3.7 References

[1] B. Zitova. Image registration methods: a survey. *Image and Vision Computing* 21, 977--1000. 2003.

[2] W. R. Crum. Non-rigid image registration: theory and practice. *British Journal of Radiology* 77, S140--S153. 2004.

[3] E. Brusseau, J. Fromageau, G. Finet, P. Delachartre and D. Vray. Axial strain imaging of intravascular data: Results on polyvinyl alcohol cryogel phantoms and carotid artery. *Ultrasound in Medicine and Biology* 27, 1631--1642. 2001.

[4] R. L. Maurice, J. Ohayon, Y. Fretigny, M. Bertrand, G. Soulez and G. Cloutier. Noninvasive vascular elastography: Theoretical framework. *IEEE Transactions on Medical Imaging* 23, 164--180. 2004.

[5] E. Brusseau, J. Kybic, J. Deprez and O. Basset. 2-D locally regularized tissue strain estimation from radio-frequency ultrasound images: theoretical developments and results on experimental data. *IEEE Transactions on Medical Imaging* 27, 145--60. 2008.

[6] D. Zikic, W. Wein, A. Khamene, D. A. Clevert and N. Navab. Fast Deformable Registration of 3D-Ultrasound Data Using a Variational Approach. *Med. Image Comp. and Comp.-Assist* 4190, 915--923. 2006.

[7] M. H. Davis, A. Khotanzad, D. P. Flamig and S. E. Harms. A physics-based coordinate transformation for 3-D image matching. *IEEE Transactions on Medical Imaging* 16, 317--28. 1997.

[8] J. F. Krucker, G. L. LeCarpentier, J. B. Fowlkes and P. L. Carson. Rapid elastic image registration for 3-D ultrasound. *IEEE transactions on medical imaging* 21, 1384--94. 2002.

[9] M. D. Craene, O. Camara and B. H. Bijnens. Large Diffeomorphic FFD Registration for Motion and Strain Quantification from 3D-US. ** 5528, 437--446. 2009.

[10] H. Zhong, T. Peters and J. V. Siebers. FEM-based evaluation of deformable image registration for radiation therapy.. *Physics in Medicine and Biology* 52, 4721--38. 2007.

[11] D. Rueckert, P. Aljabar and R. Heckemann. Diffeomorphic registration using B-splines. *MICCAI International Conference on Medical Image Computing and Computer-Assisted Intervention* 9, 702--9. 2006.

[12] B. Horn and B. Schunck. Determining optical flow. *Artificial Intelligence* 17, 185--203. 1981.

[13] T. Varghese, M. Bilgen and J. Ophir. Phase aberration effects in elastography. *Ultrasound in Medicine & Biology* 27, 819--827. 2001.

[14] T. Varghese and J. Ophir. Characterization of Elastographic Noise Using the Envelope of Echo Signals. *Ultrasound in Medicine & Biology* 24, 543--555. 1998.

[15] F. Kallel and J. Ophir. Three-dimensional tissue motion and its effect on image noise inelastography. *IEEE Transactions on Ultrasonics, Ferroelectrics and Frequency Control* , . 1997.

[16] F. Kallel and J. Ophir. A least-squares strain estimator for elastography. *Ultrasonic Imaging* 19, 195--208. 1997.

[17] T. Hall, Y. Zhu and C. Spalding. In vivo real-time freehand palpation imaging. *Ultrasound in Medicine & Biology* 29, 427--435. 2003.

[18] A. Basarab, H. Liebgott, F. Morestin, A. Lyshchik, T. Higashi, R. Asato and P. Delachartre. A method for vector displacement estimation with ultrasound imaging and its application for thyroid nodular disease. *Medical Image Analysis* 12, 259--74. 2008.

[19] J. Jiang and T. J. Hall. A parallelizable real-time motion tracking algorithm with applications to ultrasonic strain imaging. *Physics in Medicine and Biology* 52, 3773--90. 2007.

[20] H. Rivaz, E. M. Boctor, M. A. Choti and G. D. Hager. Real-Time Regularized Ultrasound Elastography. *IEEE Transactions on Medical Imaging* , 1--18. 2010.

[21] R. Zahiri-Azar and S. E. Salcudean. Motion estimation in ultrasound images using time domain cross correlation with prior estimates. *IEEE transactions on bio-medical engineering* 53, 1990--2000. 2006.

[22] L. Chen, G. M. Treece, J. E. Lindop, A. H. Gee and R. W. Prager. A quality-guided displacement tracking algorithm for ultrasonic elasticity imaging. *Medical Image Analysis* 13, 286--96. 2009.

[23] C. Pellot-Barakat, F. Frouin, M. F. Insana and A. Herment. Ultrasound elastography based on multiscale estimations of regularized displacement fields. *IEEE Transactions on Medical Imaging* 23, 153--163. 2004.

[24] H. Shi and T. Varghese. Two-dimensional multi-level strain estimation for discontinuous tissue. *Physics in Medicine and Biology* 52, 389--401. 2007.

[25] F. Yeung, S. F. Levinson and K. J. Parker. Multilevel and motion model-based ultrasonic speckle tracking algorithms. *Ultrasound in Medicine & Biology* 24, 427--442. 1998.

[26] H. Chen, H. Shi and T. Varghese. Improvement of elastographic displacement estimation using a two-step cross-correlation method. *Ultrasound in Medicine and Biology* 33, 48--56. 2007.

[27] J. Bai, C. Ding and Y. U. Fan. A multi-scale algorithm for ultrasonic strain reconstruction under moderate compression. *Ultrasonics* 37, 511--519. 1999.

[28] R. G. P. Lopata, M. M. Nillesen, H. H. G. Hansen, I. H. Gerrits, J. M. Thijssen and C. L. de Korte. Performance evaluation of methods for two-dimensional displacement and strain estimation using ultrasound radio frequency data. *Ultrasound in Medicine & Biology* 35, 796--812. 2009.

[29] A. Thitaikumar, L. M. Mobbs, C. M. Kraemer-Chant, B. S. Garra and J. Ophir. Breast tumor classification using axial shear strain elastography: a feasibility study. *Physics in Medicine and Biology* 53, 4809--23. 2008.

[30] J. Jiang and T. J. Hall. A Generalized Speckle Tracking Algorithm for Ultrasonic Strain Imaging Using Dynamic Programming. *Ultrasound in Medicine & Biology* 35, 1863--1879. 2009.

[31] H. Rivaz, E. Boctor, P. Foroughi, R. Zellars, G. Fichtinger and G. Hager. Ultrasound

elastography: a dynamic programming approach. *IEEE Transactions on Medical Imaging* 27, 1373--1377. 2008.

[32] P. M. Hayton, M. Brady, S. M. Smith and N. Moore. A non-rigid registration algorithm for dynamic breast MR images. *Artificial Intelligence* 114, 125--156. 1999.

[33] G. Xiao, J. M. Brady, J. A. Noble, M. Burcher and R. English. Nonrigid Registration of 3-D Free-Hand Ultrasound Images of the Breast. *Image Processing* 21, 405--412. 2002.

[34] J. Ophir, I. Cespedes, H. Ponnekanti, Y. Yazdi and X. Li. Elastography: a quantitative method for imaging the elasticity of biological tissues. *Ultrasonic Imaging* 13, 111--134. 1991.

[35] J. Ophir, F. Kallel, T. Varghese, E. Konofagou, S. K. S. K. Alam, T. Krouskop, B. Garra and R. Righetti. Elastography. *Comptes Rendus de l'Academie des Sciences - Series IV - Physics* 2, 1193--1212. 2001.

[36] T. S. Yoo, M. J. Ackerman, W. E. Lorensen, W. Schroeder, V. Chalana, S. Aylward, D. Metaxes and R. Whitaker. "Engineering and Algorithm Design for an Image Processing API: A Technical Report on ITK - The Insight Toolkit". In Westwood, J. (Eds.) *Medicine Meets Virtual Reality*, Amsterdam: IOS Press. 2002.

[37] Y. Li and J. A. Zagzebski. A frequency domain model for generating B-mode images with array transducers. *IEEE Transactions on Ultrasonics, Ferroelectrics, and Frequency Control* 46, . 1999.

[38] D. Cousineau. Confidence intervals in within-subject designs: A simpler solution to Loftus and Masson's method. *Tutorial in Quantitative Methods for Psychology* 1, 42--45. 2005.

[39] T. Varghese and J. Ophir. A theoretical framework for performance characterization of elastography: the strain filter. *IEEE Transactions on Ultrasonics, Ferroelectrics, and Frequency Control* 44, 164--72. 1997.

[40] A. R. Skovoroda, S. Y. Emelianov, M. A. Lubinski, A. P. Sarvazyan and M. O'Donnell. Theoretical Analysis and Verification of Ultrasound Displacement and Strain Imaging. *IEEE Transactions on Ultrasonics, Ferroelectrics and Frequency Control* 41, 302--313. 1994.

[41] R. P. Brent. *Algorithms for Minimization Without Derivatives*. Englewood Cliffs, NJ: Prentice-Hall. 1973.

[42] N. Rubert, S. Bharat, R. J. DeWall and Andreano. Electrode displacement strain imaging of thermally-ablated liver tissue in an in vivo animal model. *Medical Physics* 37, 1075. 2010.